Improved control of atomic layering in perovskite-related homologous series

Matthew R. Barone, Natalie M. Dawley, Hari P. Nair, Berit H. Goodge, Megan E. Holtz, Arsen Soukiassian, Erin E. Fleck, Kiyoung Lee, Yunfa Jia, Tassilo Heeg, Refael Gatt, Yuefeng Nie, David A. Muller, Lena F. Kourkoutis, and Darrell G. Schlom

View Online   Export Citation   CrossMark

ARTICLES YOU MAY BE INTERESTED IN

AIP Publishing HORIZONS   APL Materials   Register Today!
Materials Challenges for Memory · April 11-13, 2021 | Virtual Conference

Improved control of atomic layering in perovskite-related homologous series

View Online   Export Citation   CrossMark

Matthew R. Barone,[1,a)] (ID) Natalie M. Dawley,[1] (ID) Hari P. Nair,[1] Berit H. Goodge,[2,3] (ID) Megan E. Holtz,[1] Arsen Soukiassian,[1] Erin E. Fleck,[2] Kiyoung Lee,[4] Yunfa Jia,[1] Tassilo Heeg,[5] Refael Gatt,[6] Yuefeng Nie,[7] (ID) David A. Muller,[2,3] (ID) Lena F. Kourkoutis,[2,3] (ID) and Darrell G. Schlom[1,3,8] (ID)

AFFILIATIONS

[1] Department of Materials Science and Engineering, Cornell University, Ithaca, New York 14853, USA
[2] School of Applied and Engineering Physics, Cornell University, Ithaca, New York 14853, USA
[3] Kavli Institute at Cornell for Nanoscale Science, Ithaca, New York 14853, USA
[4] Samsung Advanced Institute of Technology (SAIT), Samsung Electronics, 130 Samsung-ro, Yeongtong-gu, Suwon-si, Gyeonggi-do 16678, South Korea
[5] Heeg Vacuum Engineering, Kerpen, Germany
[6] Quantum Designed Materials Ltd., Rehovot, Israel
[7] National Laboratory of Solid State Microstructures, College of Engineering and Applied Sciences, Collaborative Innovation Center of Advanced Microstructures, Nanjing University, Nanjing, China
[8] Leibniz-Institut für Kristallzüchtung, Max-Born-Str. 2, Berlin 12489, Germany

[a)] Author to whom correspondence should be addressed: mrb297@cornell.edu

ABSTRACT

Homologous series are layered phases that can have a range of stoichiometries depending on an index n. Examples of perovskite-related homologous series include $(ABO_3)_nAO$ Ruddlesden–Popper phases and $(Bi_2O_2)(A_{n-1}B_nO_{3n+1})$ Aurivillius phases. It is challenging to precisely control n because other members of the homologous series have similar stoichiometry and a phase with the desired n is degenerate in energy with syntactic intergrowths among similar n values; this challenge is amplified as n increases. To improve the ability to synthesize a targeted phase with precise control of the atomic layering, we apply the x-ray diffraction (XRD) approach developed for superlattices of III–V semiconductors to measure minute deviations from the ideal structure so that they can be quantitatively eradicated in subsequent films. We demonstrate the precision of this approach by improving the growth of known Ruddlesden–Popper phases and ultimately, by synthesizing an unprecedented $n = 20$ Ruddlesden–Popper phase, $(ATiO_3)_{20}AO$ where the A-site occupancy is $Ba_{0.6}Sr_{0.4}$. We demonstrate the generality of this method by applying it to Aurivillius phases and the $Bi_2Sr_2Ca_{n-1}Cu_nO_{2n+4}$ series of high-temperature superconducting phases.

I. INTRODUCTION

The growth of high quality superlattices and homologous series requires precise calibration. This is true for compound semiconductors[1] as well as complex oxides.[2] When grown by molecular-beam epitaxy (MBE), an ion gauge (beam flux monitor)[3] or quartz-crystal microbalance[4,5] can be used to get a rough measure of source fluxes, and this approximation can be improved upon by observing reflection high-energy electron diffraction (RHEED) oscillations during codeposition[6] or shuttered deposition[7–9] on a calibration sample. Unfortunately, these methods are often insufficient to consistently grow oxide superlattices and homologous series with sharp interfaces because they require not only fluxes in the right stoichiometric ratio but also the delivery of precise doses of these stoichiometric fluxes to build up the desired superlattice layering. These structures, though difficult to synthesize, are an expanding area of research.[10,11] Superlattices have long been used to realize 1D quantum wells that have proven useful engineering tools.[12] More

recently, superlattices have been found to harbor novel interfacial phenomena[13–17] and stabilize phases and strain states that would be impossible in bulk.[18–20] Interfaces in homologous series are even more complex because while atomic potentials change abruptly at superlattice interfaces, the bonding environment is completely changed at interfaces in homologous series. Ruddlesden–Popper phases, $(ABO_3)_nAO$,[21–23] are a homologous series that has been particularly fruitful, revealing high temperature and unconventional superconductivity,[24–26] colossal-magnetoresistance,[27] and record-breaking tunable dielectrics.[28,29]

The synthesis of homologous series by bulk methods is limited to those for which differences in formation energy between members of the homologous series can be used to drive the formation of phase-pure samples; these energy differences become smaller as n increases.[30–37] The Ruddlesden–Popper phases that can be produced by bulk methods are limited to low values of n (typically $n = 1, 2, 3$) and ∞, where $n = \infty$ corresponds to the perovskite end member. $n = 3$ is the highest value of n (other than $n = \infty$) that has been achieved in bulk synthesis of single-phase samples of $(SrTiO_3)_nSrO$,[38] $(SrRuO_3)_nSrO$,[39] $(CaTiO_3)_nCaO$,[40] and $(LaNiO_3)_nLaO$.[41] Indeed, transmission electron microscopy (TEM) images of attempts to make $(SrTiO_3)_nSrO$ phases with $n > 3$ show disordered syntactic intergrowths where n ranges from 2 to 8,[30] as would be expected for the bulk preparation of essentially energetically degenerate phases. The highest value of n achieved in the bulk synthesis of any oxide Ruddlesden–Popper to date is $n = 4$.[42] Interestingly, in sulfides, this limit is $n = 5$[43] and in halide perovskites is $n = 7$.[44] The preparation of high n Ruddlesden–Popper members of the halide perovskites has enabled both the electronic properties to be tuned and high efficiency solar cells with improved environmental stability to be achieved.[45]

Accessing Ruddlesden–Popper phases with intermediate n, i.e., $4 < n < \infty$ in oxide systems or other homologous series, is possible using thin-film methods by exploiting kinetics. Specifically, the order in which precise doses of the species contained in each monolayer are supplied to the substrate can build up a targeted member of a homologous series. As for bulk synthesis, high n films are more challenging, but thin films as high as $n = 10$ have been demonstrated.[46] There are subtleties involved in the order in which the monolayer doses should be supplied,[47,48] but accurate control of the monolayer doses is a prerequisite for forming these otherwise inaccessible phases. Improving the accuracy of this control is the subject of this study.

X-ray diffraction (XRD) analysis of superlattices has been developed in the III–V semiconductor community to measure the periodicity of MBE-grown quantum wells.[49] Studies found that (001)-oriented superlattices of isostructural zinc blende III–V semiconductors exhibit "zero-order peaks."[49] These peaks are analogous to the 002ℓ peaks that the pure endmembers involved in the superlattice would exhibit, where ℓ is an integer, except that in the superlattice they appear at the weighted average spacing of the constituents. For example, a commensurate superlattice containing a total of 50 GaAs layers and 150 AlAs layers will have its 004 zero-order peak at a d-spacing of $\frac{1}{4}\left(\frac{50a_{GaAs}+150a_{AlAs}}{200}\right)$, where a_{GaAs} and a_{AlAs} are the out-of-plane lattice spacings of commensurate GaAs and commensurate AlAs films grown on the same substrate as the GaAs/AlAs superlattice. In addition, each zero-order peak has nearby satellite peaks, the spacing between which indicates the out-of-plane periodicity of the

structure.[49] With this information, the average number of unit cells per supercell can be deduced, and for imperfect superlattices, this number is not an integer.

In this Letter, we first explain the utility of *ex situ* XRD to grow precise superlattices of isostructural constituents and then expand upon the technique to precisely calibrate the thin film growth of Ruddlesden–Poppers and other perovskite-related homologous series in which the grower has continuous control over the periodicity. This control is most readily achieved by adjusting deposition times, but it has also been demonstrated by pulsed-laser deposition (PLD) from a single target.[50]

II. RESULTS AND DISCUSSION

A. Isostructural superlattices

Superlattice XRD techniques are commonly applied to superlattices involving the combination of two isostructural materials, e.g., the (001)-oriented superlattice of two perovskite structures, $SrTiO_3$ and $SrRuO_3$, shown in Fig. 1(a).[51] When analyzing a superlattice with an XRD θ-2θ scan, one approach is to analyze the superlattice like a crystal with an atypically large lattice parameter in the growth direction, resulting in a short reciprocal lattice vector. This convention, denoted by vertical lines in Fig. 1(c), is sufficient to understand diffraction in well-ordered films like the blue spectrum. Such a superlattice with a well-defined unit cell [Fig. 1(a)] is, however, challenging to grow because it is not usually an equilibrium phase and errors in flux calibration result in an imperfect superlattice rather than the formation of an additional phase(s). This is true even if the stoichiometry of the film is perfect; Fig. 1(b) has perfect stoichiometry and yet, it is imperfect. The RuO_2 layers are on average 10% closer together than in Fig. 1(a), and each layer is populated by 10% less RuO_2, resulting in identical stoichiometry.

The red spectrum of Fig. 1(c) corresponds to such an imperfect superlattice for which a unit cell cannot be easily defined requiring a more flexible convention. In this convention, zero-order peaks, labeled "0," indicate the average lattice parameter of the superlattice constituents. These are typically the most intense peaks, and their location is insensitive to the superlattice periodicity. Comparing to the unit cell convention (black vertical lines), zero-order peaks correspond to multiples of the 006 reflection in $(SrTiO_3)_5SrRuO_3$ because this structure ideally has six perovskite unit cells per supercell (the transmitted beam, 000, is also a zero-order peak). Other peaks called satellite peaks are Fourier components necessary to describe the electron density of the superlattice, which resembles a square wave.[49] These satellites are labeled by their position relative to their zero-order peak as in the red spectrum of Fig. 1(c). Their spacing is sensitive to the average periodicity of the structure, which is not necessarily an integer number of perovskite unit cells [Fig. 1(b)].

We see that in the spectrum of the imperfect superlattice (red), the superlattice peaks of each zero-order peak (the peaks labeled +1, +2, +3 or −1, −2, −3) are spaced farther apart than the ideal structure, meaning that the periodicity is less than ideal. This is most obvious near the +3 satellite of 000 and the −3 satellite of 006 because these peaks ideally occupy the same position (the 003 peak of the ideal unit cell), but shift in opposite directions, resulting in a split peak. The spacing between two satellites of the same zero-order peak can be used to compute the average periodicity, Λ, of
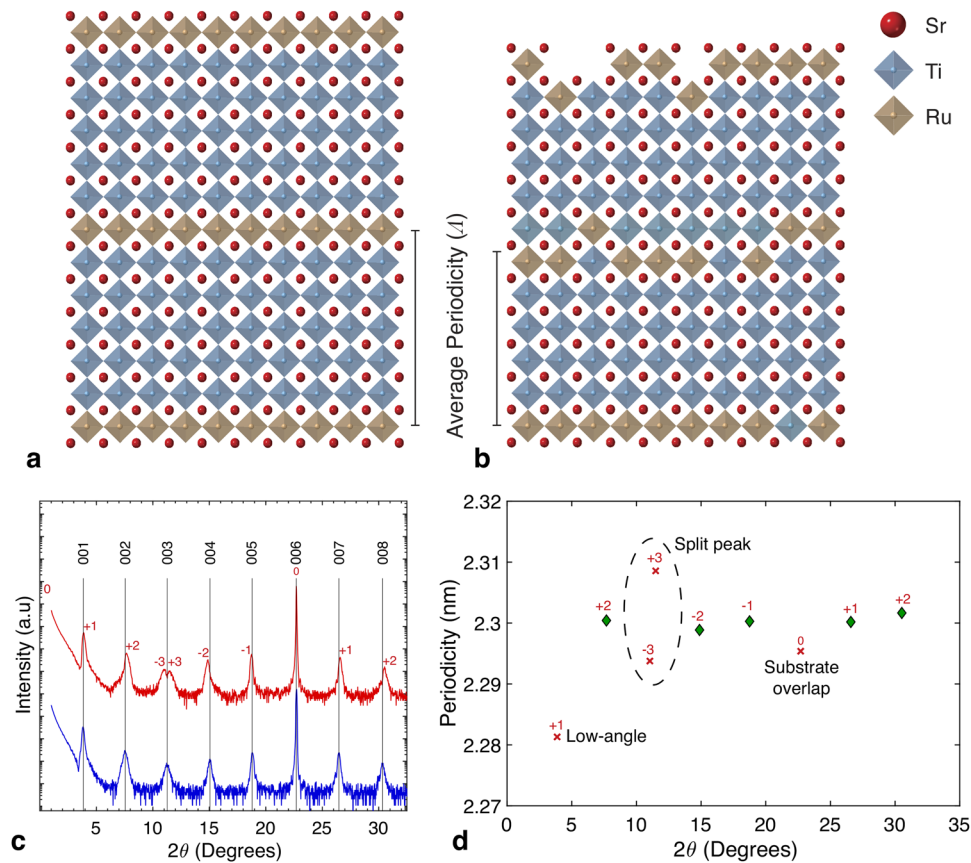
FIG. 1. (a) Structure of (SrTiO₃)₅SrRuO₃ superlattices with ideal and (b) less than ideal periodicity, $c = 0.9$ (equivalent stoichiometry). (c) θ–2θ XRD scans of 47 nm thick (SrTiO₃)₅SrRuO₃ superlattices grown on SrTiO₃ (001) substrates with ideal (blue) and less than ideal (red) periodicity.[52] (d) A plot of the periodicity predicted by each peak in the red spectrum of (c) vs 2θ at which the peak is observed. Periodicity is calculated for each peak using Eq. (3) and the correction factor that best describes the data, $c = 0.9774$. Reliable and unreliable peaks are indicated by green diamonds and red x's respectively.

the superlattice with Eq. (1), where L_i corresponds to the satellite index of peak i (labels on the red spectrum), θ_i is the location of peak i, and λ is the x-ray wavelength,[49]

$$\Lambda = \frac{(L_i - L_j)\lambda}{2[\sin(\theta_i) - \sin(\theta_j)]}. \qquad (1)$$

For example, plugging the locations of the $L_i = -2$ and $L_j = -1$ satellite peaks of the 006 zero-order peak into Eq. (1) gives a periodicity of 23.00 Å. To determine the ideal periodicity from the spectrum of an imperfect film, we use Bragg's law on the 006 zero-order peak because it is insensitive to superlattice periodicity. For calibration, it is convenient to compare the actual and ideal periodicity through a unitless correction factor, c, defined in Eq. (2), where $d_{00\ell_0}$ is the Bragg spacing of the $00\ell_0$ zero-order peak,

$$c = \frac{\Lambda}{Ideal\,\Lambda} = \frac{\Lambda}{\ell_0 d_{00\ell_0}}. \qquad (2)$$

For a perfect structure, $c = 1$. After measuring the XRD spectrum of an imperfect film ($c \neq 1$), the deposition times used to grow the imperfect film can be divided by this correction factor

to grow a film with the desired periodicity. This calibration to achieve the desired superlattice periodicity does not change the stoichiometry of the film (i.e., the ratios between the constituent atoms), only the periodicity. There are many existing *in situ* methods to optimize stoichiometry—ion gauge,[3] quartz crystal microbalance,[4,5] mass spectrometer,[53] cold cathode emission spectroscopy,[54] atomic absorption spectroscopy,[55–62] and RHEED.[7–9] Stoichiometry can also be optimized by *ex situ* measurements of composition by measuring the thickness of calibration films of the constituents. Nonetheless, these methods are less sensitive to periodicity than *ex situ* XRD. The technique described here is not intended to help optimize stoichiometry; rather it is intended to be used in conjunction with other methods that enable high control over film stoichiometry.

Using Eqs. (1) and (2) on the red spectrum in Fig. 1(c), we obtain $c = 0.980$. This indicates the film is only 2% of the ideal periodicity. Even this minute imperfection is clear by visual inspection of the spectrum showing the sensitivity of the technique. In practice, applying this method can have complications, one of the most common being the influence of the substrate skewing the apparent location of the zero-order peak.

To circumvent this issue, it is helpful to rearrange Eqs. (1) and (2) such that they do not require precise determination of the zero-order peak's location. The periodicity of a superlattice with a known correction factor, c, can be calculated from a single satellite peak by combining Eqs. (1) and (2). The result of this algebra (shown in more detail in the supplementary material) is Eq. (3), where peak i is a satellite of $00\ell_0$, and c is a known (or assumed) value,

$$\Lambda_i = \frac{(L_i + \ell_0 c)\lambda}{2\sin(\theta_i)}. \tag{3}$$

In Eq. (3), the value of c that best describes the film should yield the same periodicity for all superlattice peaks not skewed by the substrate or other factors. Searching for the c value that yields the most consistent Λ_i across all reliable superlattice peaks enables us to determine a more accurate correction factor for each film. Applying this self-consistent approach to the red spectrum in Fig. 1(c) yields a value of $c = 0.9774 \pm 0.0004$, compared to $c = 0.980$ computed with Eqs. (1) and (2).

In Fig. 1(d), the result of Eq. (3) is plotted for each satellite peak using the optimized correction factor $c = 0.9774$. This figure highlights the different reasons peaks may be justifiably omitted from the analysis. We find that low-angle ($2\theta \lesssim 10°$) satellite peaks, hard-to-deconvolute split peaks, and peaks that overlap with the substrate are often inconsistent with the rest of the data,[63] all of which are observed in this spectrum. The power of Eq. (3) is primarily that it enables these unreliable peaks to be identified and excluded. In addition, it allows a statistical analysis of the uncertainty of the periodicity measurement. While more informative, at least three, ideally more, superlattice peaks are required for this method to be advantageous. Using only two peaks is equivalent to drawing a line of best fit through two points, and provides no more information than Eqs. (1) and (2). Using three peaks is slightly better but still makes objective omission of unreliable peaks difficult, which is the primary advantage of the method.

A simple program is included in the supplementary material that determines the c value with error bars that best describe a film for user-defined satellite locations about a single zero-order peak. This code plots the data similarly to Fig. 1(d) to help the user identify and explain which superlattice peaks are inconsistent so that they can be omitted from the analysis. Having developed the tools to analyze the XRD pattern of a relatively simple oxide superlattice, we now move on to the more challenging analysis of Ruddlesden–Popper phases.

B. Ruddlesden–Popper series

In contrast to superlattices of isostructural constituents, (001)-oriented Ruddlesden–Popper films, $(ABO_3)_nAO$, consist of n perovskite unit cells and one half of a rock salt unit cell (one monolayer of rock salt) as seen in Fig. 2(a). Because a monolayer of rock salt (2.57 Å thick for SrO) and a half of a perovskite unit cell (1.95 Å thick for SrTiO₃) have comparable dimensions and Ruddlesden–Popper structures contain two formula units per unit cell, they have a zero-order peak at $004\underline{n+2}$ corresponding to the average monolayer spacing, which is insensitive to periodicity. Although superlattice analysis can be performed on any Ruddlesden–Popper film, the $n = 1$ Ruddlesden–Popper Sr₂TiO₄ is attractive for calibration because satellite peaks are easily visible even for highly imperfect

films less than 30 nm thick. Figure 2(b) shows typical XRD spectra of Sr₂TiO₄ grown by alternately shuttering ~2 monolayers of SrO and ~1 monolayer of TiO₂ after optimizing stoichiometry within ~1% (see the supplementary material). The θ–2θ XRD scans resemble the superlattice XRD in Fig. 1(c) where—coincidentally—000 and 006 are again the zero-order peaks.

Near the ideal 002 peak, we consistently see the +2 satellite of 000, and in some cases, the −4 satellite of 006 is also observable. These peaks occupy the same position in a perfect structure, but they shift in opposite directions with deviations from ideal shutter time akin to the splitting seen for the 003 peak of $(SrTiO_3)_5SrRuO_3$ in Fig. 1(c). Similarly, the 004 peak splits into the −2 satellite of 006 and the sometimes observable +4 satellite of 000.

The defects enabling a Ruddlesden–Popper of noninteger periodicity are not as clear as those of the isostructural $(SrTiO_3)_5SrRuO_3$ superlattice [Fig. 1(b)] in which imprecise shuttering could be accommodated with substitutional defects. The most obvious defect structure would be periodic intergrowths of different members of the Ruddlesden–Popper series, but this implies deviations in stoichiometry, which is not the subject of this study, and fails to explain films with c-axis periodicity shorter than the $n = 1$ structure. Another defect structure that has been observed previously in $n = 1$ Ruddlesden–Popper films[64] is the out-of-phase boundaries depicted in Fig. 2(a). Two types of boundaries are shown corresponding to shutter times that are either too long or too short, where the phase above the boundary is shifted by $\left[\frac{1}{2}, \frac{1}{2}, \frac{1}{6}\right]$ or $\left[\frac{1}{2}, \frac{1}{2}, -\frac{1}{6}\right]$ of an $n = 1$ unit cell, respectively. These predicted defects are supported by structure factor calculations along the growth direction, which are consistent with experimental observation [Figs. 2(b) and 2(c)].

Independent of the precise defect structure, the trend can be leveraged to compute the absolute fluxes of Ruddlesden–Popper constituents after stoichiometry has been optimized, analogous to isostructural superlattices. While Eq. (3) may have been used to find the optimum correction factor for each film, the primary advantage of Eq. (3) is to omit unreliable peaks, and the presence of only 3 consistently visible peaks makes unbiased omission impossible. Therefore, the actual periodicity was computed by inserting 000 and its +2 satellite as well as 006 and its −2 satellite into Eq. (1)[49] and averaging the two. This periodicity and the ideal periodicity, $6d_{006}$, determined from the zero-order peak were used to compute a correction factor, c [Eq. (2)], and the shutter times used in the growth of the imperfect film were divided by c to improve the film synthesis recipe. As for isostructural superlattices, this adjustment does not change the stoichiometry of the film, only the periodicity.

Figures 3(a) and 3(b) show that the shift in the peak position of the 002 and 004 peaks (i.e., the +2 satellite of 000 and the −2 satellite of 006, respectively) are generally consistent with expectation in the growth of over 100 samples; a dot on the red line implies that the two pairs of peaks measure identical periodicity. In this figure, the satellite peak Bragg spacings are both normalized by d_{006} because they are proportional to the average monolayer spacing, which may vary with slight off-stoichiometry or substrate choice because the films are commensurately strained. Notice that there is a deviation from the red line in Figs. 3(a) and 3(b); this arises because the only satellite peaks available are often split and hard to deconvolute. Unfortunately, there are not enough reliable peaks to permit the omission of the unreliable ones. Even given this drawback, it is clear
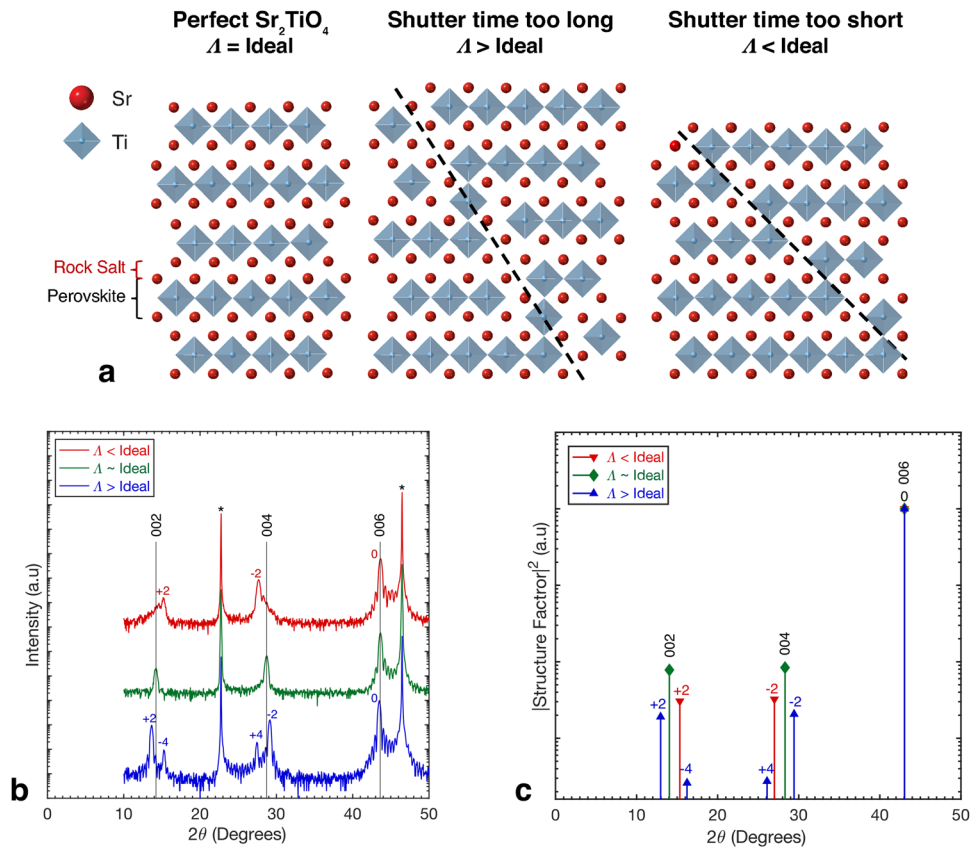
FIG. 2. (a) Possible defect structures for Sr_2TiO_4 films grown with imprecise shuttering. (b) Experimental θ–2θ XRD scans of Sr_2TiO_4 films grown with imprecise shuttering. The asterisk "∗" denotes the 001 peak of the $SrTiO_3$ substrate. (c) Computed structure factors for defect structures in (a) normalized to the 006 peak.

from the strong correlation seen in Figs. 3(a) and 3(b) that valuable information can be gleaned from the imperfect data.

The calibration method is validated by the growth of a $(SrTiO_3)_{10}SrO$ sample. This sample was grown immediately after analyzing the XRD of a Sr_2TiO_4 film to precisely determine the appropriate shutter times. The XRD of the resulting film is shown in Fig. 3(c). Clearly resolved satellite peaks consistent with an $n = 10$ phase are evident. The same film was also investigated by low-angle annular dark field scanning transmission electron microscopy (LAADF-STEM), and the result is shown in Fig. 3(d). In addition to the expected horizontally oriented double AO Ruddlesden–Popper faults, vertically oriented double AO layers are also seen. The unintended vertical faults revealed STEM are present in almost all Ruddlesden–Popper films with $n > 2$.[28,29,46,48,65–70] They are also present in the growth of bulk Ruddlesden–Popper phases with $n > 1$.[71–75] They can conceivably be caused by a multitude of factors (e.g., imperfect film stoichiometry, imperfect substrate surface stoichiometry, substrate terraces, and kinetic limitations) in addition to imperfect periodicity, and they are increasingly difficult to eradicate as n increases, which is why there are no reports of Ruddlesden–Poppers with $n > 10$.[46]

Rather than growing a calibration sample before attempting to grow a challenging structure, this technique can be used to correct the periodicity directly for the Ruddlesden–Popper of interest, enabling the grower to iteratively correct the structure. This is most practical for low n Ruddlesden–Poppers, in which satellite peaks are visible with large errors in shutter time (up to at least 15%) and short growths (∼20 nm). Figure 4(a) shows the XRD patterns of $(SrSnO_3)_2SrO$ films grown sequentially, where the shutter times were iteratively improved between films. Here, the use of Eq. (3) is appropriate because there are enough visible peaks to identify outliers, which in this case included the low-angle +2 satellite of the 000 peak and the satellites making up the split 004 peak. Using our calibration technique, the error in periodicity is reduced by about an order of magnitude from sample 1 to sample 2 and essentially disappears in sample 3, which was subsequently characterized with high-angle annular dark field scanning transmission electron microscopy (HAADF-STEM) confirming the impeccable structural quality [Fig. 4(b)].

In addition to improving the quality and consistency with which previously demonstrated Ruddlesden–Poppers can be grown, we apply the superlattice methodology to grow a new Ruddlesden–Popper: $(ATiO_3)_{20}AO$ where the A-site occupancy is 60%Ba:40%Sr. An $n = 20$ structure is hard to grow because its periodicity and stoichiometry are both very similar to adjacent
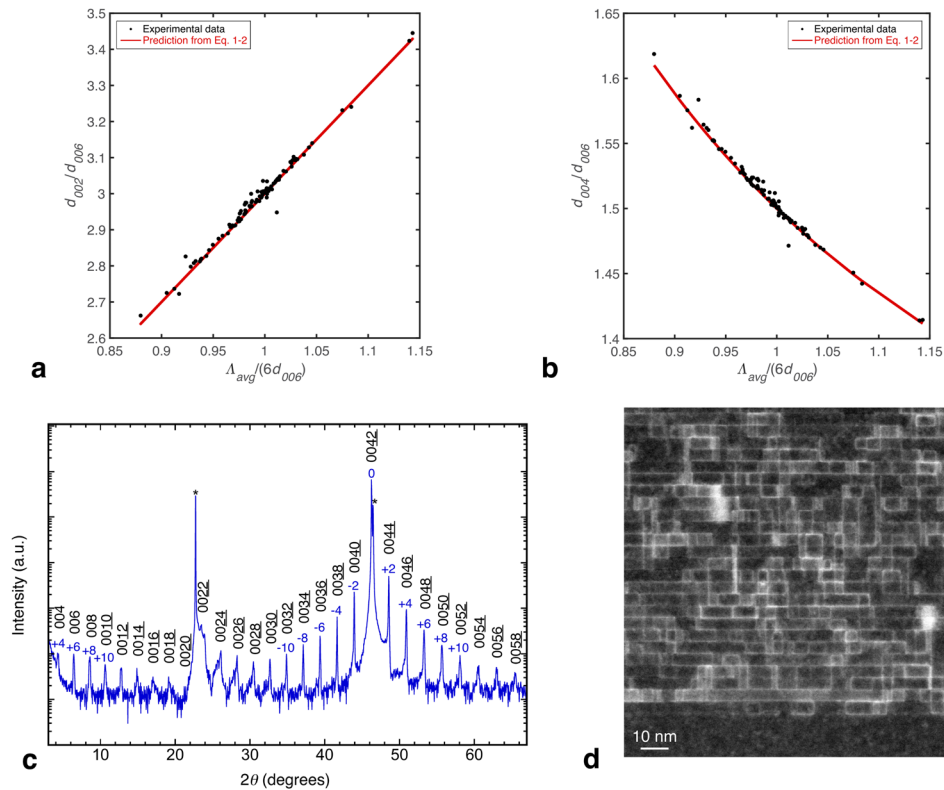
FIG. 3. Plots of the (a) 002 and (b) 004 Bragg spacing normalized by the 006 spacing vs correction factor from XRD data from the growth of over 100 Sr_2TiO_4 films (typically 25 nm thick). Black dots are experimental Bragg spacing plotted against the average correction factor computed from both sets of peaks and red lines indicate the anticipated trend from combining Eqs. (1) and (2). (c) θ–2θ XRD scan of a 300 nm thick $(SrTiO_3)_{10}SrO$ film grown on $SrTiO_3$. The asterisk "∗" denotes the peaks from the $SrTiO_3$ substrate. (d) LAADF-STEM of the same $(SrTiO_3)_{10}SrO$ film.

series members. The highest n Ruddlesden–Popper oxide phase that has ever been prepared in bulk has $n = 4$.[42] The highest n that has ever been reported in a thin film is $(SrTiO_3)_{10}SrO$ with $n = 10$.[46] Furthermore, a $(BaTiO_3)_nBaO$ Ruddlesden–Popper phase has never been synthesized, only disordered RP faults,[76] due to the competing phase barium orthotitanate (Ba_2TiO_4), which is not a Ruddlesden–Popper.[77,78] This competing phase makes incorporation of barium into the Ruddlesden–Popper structure
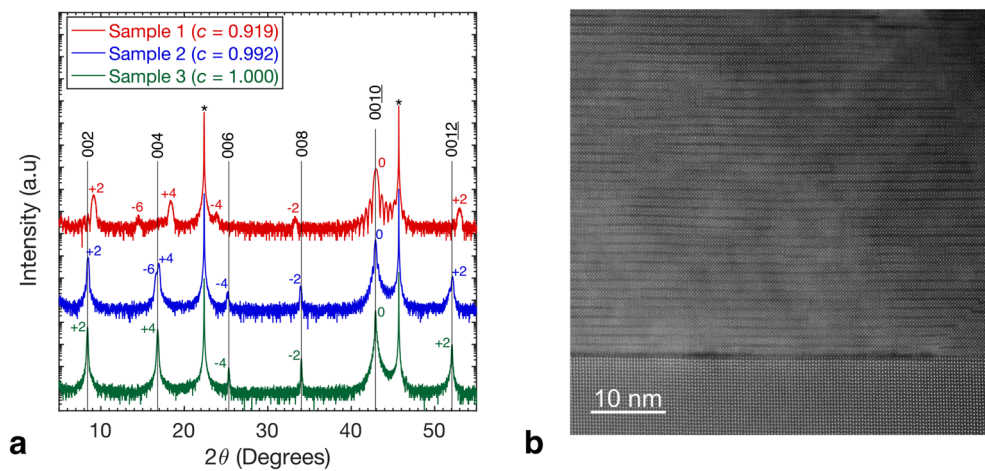

FIG. 4. (a) θ–2θ XRD scans of three consecutive $(SrSnO_3)_2SrO$ films grow on $GdScO_3$ (110) and iteratively improved. The asterisk "∗" denotes the peaks from the substrate. (b) HAADF-STEM of sample 3, (a) $(SrSnO_3)_2SrO$ film within 0.1% of ideal periodicity.

challenging, despite interest for new ferroelectrics and low-loss tunable dielectrics.[29]

To accomplish a highly ordered $(A\mathrm{TiO}_3)_{20}AO$ structure, 55 nm thick films of the $n = 20$ structure were grown, iteratively; $n = 1$ calibration films with this A-site stoichiometry were not attempted because $\mathrm{Ba}_2\mathrm{TiO}_4$ is more likely to precipitate in low n films. The first attempt, shown in red in Fig. 5(a), had a shutter time ~2% too short, determined by optimizing Eq. (3) and omitting the $00\underline{82}$ zero-order peak, which was skewed by the substrate. Judging from *in situ* RHEED and the low intensity of satellites, the film was also ~1% A-site deficient. While stoichiometric optimization was critical for this synthesis, it is unrelated to the XRD calibration technique that is the subject of this paper, so further details are located in the supplementary material. In the second film (blue), the shutter times were increased asymmetrically (i.e., A-site times were increased by 2.5% and the Ti time was increased by 1.5%) to resolve stoichiometry while approaching the ideal periodicity. With both stoichiometry and periodicity near optimal in sample 2 of Fig. 5(a), we finally synthesized a 125 nm thick $(A\mathrm{TiO}_3)_{20}AO$ ($A = \mathrm{Sr}_{.0.4}\mathrm{Ba}_{0.6}$) film with periodicity accurate to better than 0.5% [green spectrum in Figs. 5(a) and 5(b)] as determined by use of Eq. (3) on the XRD spectrum (again omitting the $00\underline{82}$ zero-order peak). The precision of the synthesis is further reinforced by strain mapping a medium-angle annular dark field (MAADF)-STEM image of this film [Figs. 5(c) and 5(d)]. Mapping the strain along the z-axis can be used to identify the location of horizontal Ruddlesden–Popper faults because the vertical spacing between two AO layers is greater than that between an AO layer and a TiO_2 layer (more details are available in the supplementary material). Statistical analysis of the strain map shows that the $n = 20$ Ruddlesden–Popper is the dominant phase and nearby n

phases ($n = 19, 21$) or phases with around double or triple the periodicity ($n = 41, 61$) are also observed as expected for higher n members of the homologous series that are well lattice-matched to the $n = 20$ matrix of the sample.[67] While the growth of this complex and interesting structure is an impressive feat on its own, our methodology enables the synthesis of such films consistently, facilitating efficient investigation of dielectric and ferroelectric properties of these new $(A\mathrm{TiO}_3)_nAO$ compounds.

In summary, after the relative flux of constituent elements has been determined, it is possible to calibrate the absolute flux of those elements by performing this XRD analysis on any member of the Ruddlesden–Popper series. Calibrating with low n Ruddlesden–Popper films has the advantage that these films are easier to synthesize, but calibrating with low n members, particularly $n = 1$, has the disadvantage that there are fewer peaks to analyze preventing the omission of unreliable peaks with Eq. (3). Even with this drawback, in our experience, the inaccuracy rarely exceeds 1%, which is a significant improvement in accuracy of other calibration techniques, enabling synthesis of the $n = 10$ Ruddlesden–Popper in Figs. 3(c) and 3(d). We have also demonstrated that it is possible to use this method directly on the high n Ruddlesden–Popper of interest, but as n increases the differences in periodicity, stoichiometry, and formation energy between adjacent members decreases. As a result, even small errors can result in no visible satellites preventing the use of the proposed XRD calibration method.

III. OTHER HOMOLOGOUS SERIES

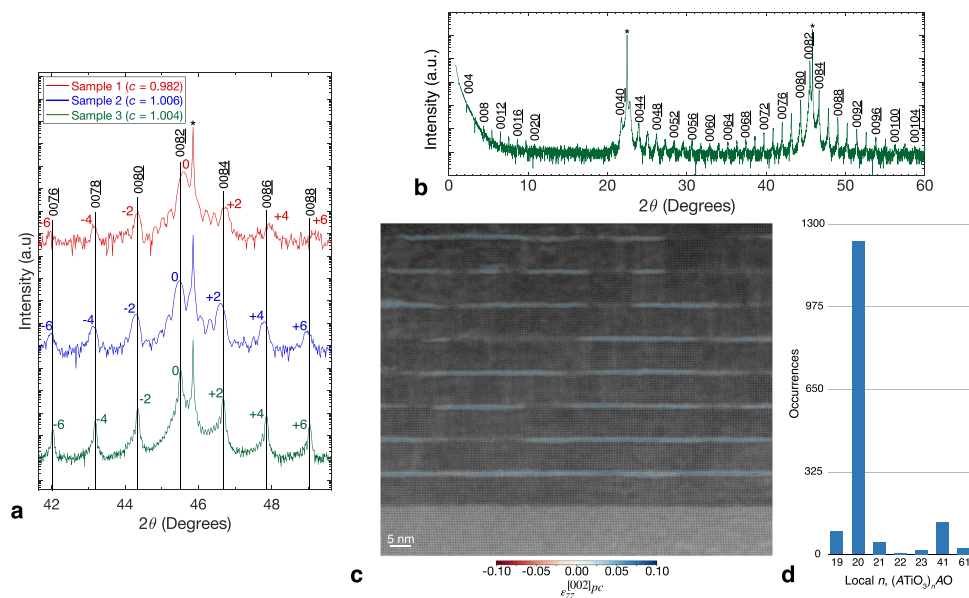In addition to superlattices and Ruddlesden–Popper thin films, we find evidence that the same concept can be used for

FIG. 5. (a) θ–2θ XRD scans of three consecutive $(A\mathrm{TiO}_3)_{20}AO$ films grown on TbScO_3 (110). (b) θ–2θ XRD scan of optimized $(A\mathrm{TiO}_3)_{20}AO$ film. (c) MAADF-STEM of optimized $(A\mathrm{TiO}_3)_{20}AO$ film with strain map overlay to highlight Ruddlesden–Popper faults. The local transparency of the overlaid strain map is proportional to the strain amplitude such that large strain amplitudes are more opaque and small amplitudes are more transparent. (d) Bar graph showing the prevalence of different Ruddlesden–Popper phases in (c) (n not shown had zero occurrences).
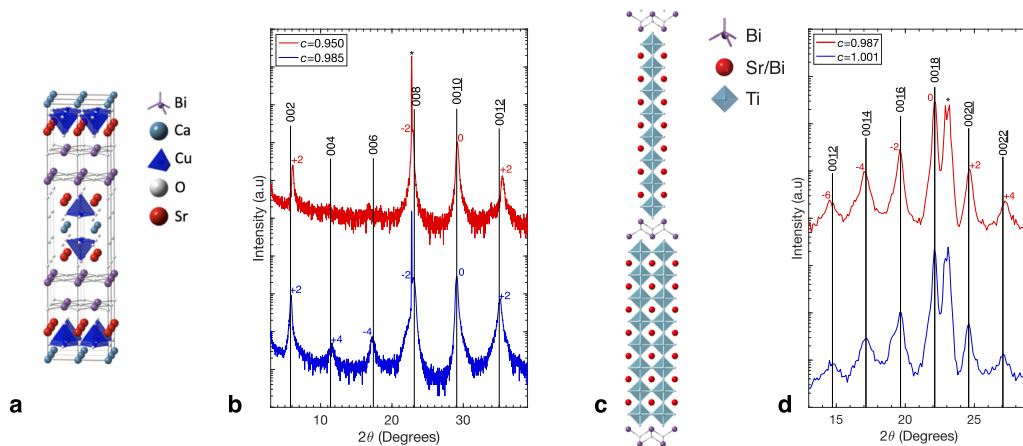
FIG. 6. (a) Structure of Bi-2212. (b) θ–2θ XRD scans of Bi-2212 thin films grown on SrTiO$_3$ with different errors in shutter time. The asterisk "*" denotes the peaks from the substrate. (c) Structure of an $n = 8$ Aurivillius phase, Sr$_5$Bi$_4$Ti$_8$O$_{27}$. (d) θ–2θ XRD scan of two Aurivillius films grown by single-target pulsed-laser deposition on NdGaO$_3$ (110).

other homologous series grown by shuttering such as the Bi$_2$Sr$_2$Ca$_{n-1}$Cu$_n$O$_{2n+4}$ (BSCCO) series of high-temperature superconducting phases.[79] As can be seen in Fig. 6(b), the red XRD spectrum cannot be explained as single phase $n = 2$ (Bi-2212) [Fig. 6(a)] nor as a random mixture of two BSSCO phases. While we have not attempted to use the XRD calibration technique demonstrated for superlattices and Ruddlesden–Poppers to correct BSCCO films, we conclude from the appearance of zero-order and satellite peaks in these shuttered films that such calibration is likely possible. The imprecise shuttering of the constituent elements may create out-of-phase boundaries (as posited for Ruddlesden–Popper films) or periodic intergrowths of the $n = 1$ phase, Bi-2201, since the stoichiometry of this complex phase is harder to control. In $n \approx 2$ films, the 0010 appears least sensitive to shutter time, meaning this peak is best used as the zero-order peak. We believe it is least sensitive because the $n = 1$ and $n = 3$ spectra have 008 and 0012 peaks, respectively, at nearly the same 2θ.[80] For these spectra, correction factors were computed using Eqs. (1) and (2) on the 0010 zero-order peak and its +2 satellite because there are not enough peaks to enable the identification of outliers with Eq. (3), but these peaks are the most likely to be reliable.

We also analyze the XRD data of $n \approx 8$ Aurivillius films,[81–85] Sr$_5$Bi$_4$Ti$_8$O$_{27}$, grown by single-target PLD [Figs. 6(c) and 6(d)]. Aurivillius phases, with the general formula (Bi$_2$O$_2$) ($A_{n-1}B_n$O$_{3n+1}$), consist of n perovskite unit cells (each 3.905 Å thick for SrTiO$_3$) separated by Bi$_2$O$_2^{2-}$ layers (4.47 Å thick for SrBi$_4$Ti$_4$O$_{15}$). Similar to Ruddlesden–Poppers, there are still two formula units per Sr$_5$Bi$_4$Ti$_8$O$_{27}$ unit cell, but the Bi$_2$O$_2^{2-}$ layers have a comparable thickness to an entire perovskite unit cell—not just a half of the perovskite unit cell as was the case for rock salt layers. The resulting zero-order peaks are at multiples of the 002n + 2 reflection, or the 0018, 0036, and 0054 peaks in the $n = 8$ structure. Here, there are plenty of peaks to enable the use of Eq. (3) on the θ–2θ XRD scans in Fig. 6(d), allowing us to determine that the 0018 zero-order peak is skewed by the substrate, justifying its omission from the

analysis. We find that the periodicity of Aurivillius films can vary continuously, again suggesting that this *ex situ* XRD calibration may be useful. Since this structure was grown with a single target, correction is not as straightforward as shutter-controlled MBE, but it has been demonstrated that the periodicity of Ruddlesden–Popper or Aurivillius-phase films can be controlled with single-target PLD by changing the growth rate,[50] or film deposition temperature (where the volatility of a component can be used to change the film composition),[86–89] suggesting that calibration is possible, albeit challenging.

IV. CONCLUSION

We have expanded the methodology for analyzing the θ–2θ XRD patterns of superlattices to enable precise synthesis of homologous series in addition to isostructural superlattices. This calibration strategy has been validated by the synthesis of highly ordered Ruddlesden–Popper films, including an unprecedented $n = 20$ structure, and we provide substantial evidence that the same strategy can be leveraged for other homologous series. By improving the precision and consistency with which targeted complex structures are synthesized with atomic-layer precision, we anticipate that the physical properties of previously unattainable structures may begin to be explored.

SUPPLEMENTARY MATERIAL

See the supplementary material for more details on synthesis and characterization. Synthetic description of substrate preparation, stoichiometry optimization, and other growth details are included. In addition, there is further discussion on the analysis of superlattice XRD particularly the implementation of Nelson–Riley analysis[90] and the appearance of additional zero-order peaks (e.g., at 002n + 1) in some Ruddlesden–Popper films with $n > 4$. Further details regarding strain mapping of STEM images are also included.

DATA AVAILABILITY

The data that support the findings of this study are available from the corresponding author upon reasonable request.

REFERENCES

[1] A. C. Gossard, P. M. Petroff, W. Weigmann, R. Dingle, and A. Savage, Appl. Phys. Lett. **29**, 323 (1976).

[2] D. G. Schlom, L.-Q. Chen, X. Pan, A. Schmehl, and M. A. Zurbuchen, J. Am. Ceram. Soc. **91**, 2429 (2008).

[3] G. R. Giedd and M. H. Perkins, Rev. Sci. Instrum. **31**, 773 (1960).

[4] G. n. Sauerbrey, Z. Phys. **155**, 206 (1959).

[5] H. K. Pulker and J. P. Decosterd, in *Applied Piezoelectric Quartz Crystal Microbalances*, edited by C. Lu and A. W. Czanderna (Elsevier, 1984), pp. 63–123.

[6] J. J. Harris, B. A. Joyce, and P. J. Dobson, Surf. Sci. **103**, L90 (1981).

[7] J. H. Haeni, C. D. Theis, and D. G. Schlom, J. Electroceram. **4**, 385 (2000).

[8] H. Y. Sun, Z. W. Mao, T. W. Zhang, L. Han, T. T. Zhang, X. B. Cai, X. Guo, Y. F. Li, Y. P. Zang, W. Guo, J. H. Song, D. X. Ji, C. Y. Gu, C. Tang, Z. B. Gu, N. Wang, Y. Zhu, D. G. Schlom, Y. F. Nie, and X. Q. Pan, Nat. Commun. **9**, 2965 (2018).

[9] G. Vinai, F. Motti, A. Y. Petrov, V. Polewczyk, V. Bonanni, R. Edla, B. Gobaut, J. Fujii, F. Suran, D. Benedetti, F. Salvador, A. Fondacaro, G. Rossi, G. Panaccione, B. A. Davidson, and P. Torelli, Rev. Sci. Instrum. **91**, 085109 (2020).

[10] J. Mannhart and D. G. Schlom, Science **327**, 1607 (2010).

[11] H. Y. Hwang, Y. Iwasa, M. Kawasaki, B. Keimer, N. Nagaosa, and Y. Tokura, Nat. Mater. **11**, 103 (2012).

[12] L. Esaki, IEEE J. Quantum Electron. **22**, 1611 (1986).

[13] P. A. Salvador, A.-M. Haghiri-Gosnet, B. Mercey, M. Hervieu, and B. Raveau, Appl. Phys. Lett. **75**, 2638 (1999).

[14] A. Ohtomo, D. A. Muller, J. L. Grazul, and H. Y. Hwang, Nature **419**, 378 (2002).

[15] M. Huijben, G. Rijnders, D. H. A. Blank, S. Bals, S. V. Aert, J. Verbeeck, G. V. Tendeloo, A. Brinkman, and H. Hilgenkamp, Nat. Mater. **5**, 556 (2006).

[16] A. Bhattacharya, S. J. May, S. G. E. te Velthuis, M. Warusawithana, X. Zhai, B. Jiang, J.-M. Zuo, M. R. Fitzsimmons, S. D. Bader, and J. N. Eckstein, Phys. Rev. Lett. **100**, 257203 (2008).

[17] P. Moetakef, T. A. Cain, D. G. Ouellette, J. Y. Zhang, D. O. Klenov, A. Janotti, C. G. Van de Walle, S. Rajan, S. J. Allen, and S. Stemmer, Appl. Phys. Lett. **99**, 232116 (2011).

[18] W. Tian, J. C. Jiang, X. Q. Pan, J. H. Haeni, Y. L. Li, L. Q. Chen, D. G. Schlom, J. B. Neaton, K. M. Rabe, and Q. X. Jia, Appl. Phys. Lett. **89**, 092905 (2006).

[19] J. A. Mundy, C. M. Brooks, M. E. Holtz, J. A. Moyer, H. Das, A. F. Rébola, J. T. Heron, J. D. Clarkson, S. M. Disseler, Z. Liu, A. Farhan, R. Held, R. Hovden, E. Padgett, Q. Mao, H. Paik, R. Misra, L. F. Kourkoutis, E. Arenholz, A. Scholl, J. A. Borchers, W. D. Ratcliff, R. Ramesh, C. J. Fennie, P. Schiffer, D. A. Muller, and D. G. Schlom, Nature **537**, 523 (2016).

[20] W. Geng, X. Guo, Y. Zhu, Y. Tang, Y. Feng, M. Zou, Y. Wang, M. Han, J. Ma, B. Wu, W. Hu, and X. Ma, ACS Nano **12**, 11098 (2018).

[21] D. Balz and K. Plieth, Z. Elektrochem. **59**, 545 (1955).

[22] S. N. Ruddlesden and P. Popper, Acta Crystallogr. **10**, 538 (1957).

[23] S. N. Ruddlesden and P. Popper, Acta Crystallogr. **11**, 54 (1958).

[24] H. Müller-Buschbaum, Angew. Chem., Int. Ed. Engl. **28**, 1472 (1989).

[25] Y. Maeno, H. Hashimoto, K. Yoshida, S. Nishizaki, T. Fujita, J. G. Bednorz, and F. Lichtenberg, Nature **372**, 532 (1994).

[26] A. P. Mackenzie and Y. Maeno, Rev. Mod. Phys. **75**, 657 (2003).

[27] Y. Moritomo, A. Asamitsu, H. Kuwahara, and Y. Tokura, Nature **380**, 141 (1996).

[28] C.-H. Lee, N. D. Orloff, T. Birol, Y. Zhu, V. Goian, E. Rocas, R. Haislmaier, E. Vlahos, J. A. Mundy, L. F. Kourkoutis, Y. Nie, M. D. Biegalski, J. Zhang, M. Bernhagen, N. A. Benedek, Y. Kim, J. D. Brock, R. Uecker, X. X. Xi, V. Gopalan, D. Nuzhnyy, S. Kamba, D. A. Muller, I. Takeuchi, J. C. Booth, C. J. Fennie, and D. G. Schlom, Nature **502**, 532 (2013).

[29] N. M. Dawley, E. J. Marksz, A. M. Hagerstrom, G. H. Olsen, M. E. Holtz, V. Goian, C. Kadlec, J. Zhang, X. Lu, J. A. Drisko, R. Uecker, S. Ganschow, C. J. Long, J. C. Booth, S. Kamba, C. J. Fennie, D. A. Muller, N. D. Orloff, and D. G. Schlom, Nat. Mater. **19**, 176 (2020).

[30] R. J. D. Tilley, J. Solid State Chem. **21**, 293 (1977).

[31] K. R. Udayakumar and A. N. Cormack, J. Am. Ceram. Soc. **71**, C469 (1988).

[32] K. R. Udayakumar and A. N. Cormack, J. Phys. Chem. Solids **50**, 55 (1989).

[33] H. Yokokawa, N. Sakai, T. Kawada, and M. Dokiya, J. Solid State Chem. **94**, 106 (1991).

[34] K. T. Jacob, K. T. Lwin, and Y. Waseda, J. Electrochem. Soc. **150**, E227 (2003).

[35] K. T. Jacob, K. Thi Lwin, and Y. Waseda, Mater. Sci. Eng. B **103**, 152 (2003).

[36] A. Banerjee, R. Prasad, and V. Venugopal, J. Alloys Compd. **373**, 59 (2004).

[37] M. Zinkevich, N. Solak, H. Nitsche, M. Ahrens, and F. Aldinger, J. Alloys Compd. **438**, 92 (2007).

[38] G. J. McCarthy, W. B. White, and R. Roy, J. Am. Ceram. Soc. **52**, 463 (1969).

[39] E. Carleschi, B. P. Doyle, R. Fittipaldi, M. Granata, A. M. Strydom, M. Cuoco, and A. Vecchione, Phys. Rev. B **90**, 205120 (2014).

[40] M. M. Elcombe, E. H. Kisi, K. D. Hawkins, T. J. White, P. Goodman, and S. Matheson, Acta Crystallogr. Sect. B **47**, 305 (1991).

[41] R. A. M. Ram, L. Ganapathi, P. Ganguly, and C. N. R. Rao, J. Solid State Chem. **63**, 139 (1986).

[42] S. Liu, M. Avdeev, Y. Liu, M. R. Johnson, and C. D. Ling, Inorg. Chem. **55**, 1403 (2016).

[43] B. H. Chen, B. W. Eichhorn, and P. E. Fanwick, Inorg. Chem. **31**, 1788 (1992).

[44] C. M. M. Soe, G. P. Nagabhushana, R. Shivaramaiah, H. Tsai, W. Nie, J.-C. Blancon, F. Melkonyan, D. H. Cao, B. Traoré, L. Pedesseau, M. Kepenekian, C. Katan, J. Even, T. J. Marks, A. Navrotsky, A. D. Mohite, C. C. Stoumpos, and M. G. Kanatzidis, Proc. Natl. Acad. Sci. U. S. A. **116**, 58 (2019).

[45] I. Spanopoulos, I. Hadar, W. Ke, Q. Tu, M. Chen, H. Tsai, Y. He, G. Shekhawat, V. P. Dravid, M. R. Wasielewski, A. D. Mohite, C. C. Stoumpos, and M. G. Kanatzidis, J. Am. Chem. Soc. **141**, 5518 (2019).

[46] C.-H. Lee, N. J. Podraza, Y. Zhu, R. F. Berger, S. Shen, M. Sestak, R. W. Collins, L. F. Kourkoutis, J. A. Mundy, H. Wang, Q. Mao, X. Xi, L. J. Brillson, J. B. Neaton, D. A. Muller, and D. G. Schlom, Appl. Phys. Lett. **102**, 122901 (2013).

[47] J. H. Lee, G. Luo, I. C. Tung, S. H. Chang, Z. Luo, M. Malshe, M. Gadre, A. Bhattacharya, S. M. Nakhmanson, J. A. Eastman, H. Hong, J. Jellinek, D. Morgan, D. D. Fong, and J. W. Freeland, Nat. Mater. **13**, 879 (2014).

[48] Y. F. Nie, Y. Zhu, C. H. Lee, L. F. Kourkoutis, J. A. Mundy, J. Junquera, P. Ghosez, D. J. Baek, S. Sung, X. X. Xi, K. M. Shen, D. A. Muller, and D. G. Schlom, Nat. Commun. **5**, 4530 (2014).

[49] D. K. Bowen and B. K. Tanner, *High Resolution X-Ray Diffractometry and Topography* (CRC Press, 1998).

[50] R. Takahashi, K. Valset, E. Folven, E. Eberg, J. K. Grepstad, and T. Tybell, Appl. Phys. Lett. **97**, 081906 (2010).

[51] M. Warusawithana, *Heteroepitaxial Interfaces Modify Collective States in Complex Oxides* (University of Illinois at Urbana-Champaign, 2005).

[52] H. Boschker, T. Harada, T. Asaba, R. Ashoori, A. V. Boris, H. Hilgenkamp, C. R. Hughes, M. E. Holtz, L. Li, D. A. Muller, H. Nair, P. Reith, X. Renshaw Wang, D. G. Schlom, A. Soukiassian, and J. Mannhart, Phys. Rev. X **9**, 011027 (2019).

[53] L. L. Chang, L. Esaki, W. E. Howard, and R. Ludeke, J. Vac. Sci. Technol. **10**, 11 (1973).

[54] J. Sakai, G. Chen, K. Hirama, S.-i. Murakami, and T. Ishida, Jpn. J. Appl. Phys., Part 1 **27**, 319 (1988).

[55] A. J. Stirling and W. D. Westwood, J. Appl. Phys. **41**, 742 (1970).

[56] T. Y. Kometani and W. Wiegmann, J. Vac. Sci. Technol. **12**, 933 (1975).

[57] M. E. Klausmeier-Brown, J. N. Eckstein, I. Bozovic, and G. F. Virshup, Appl. Phys. Lett. **60**, 657 (1992).

[58] S. J. Benerofe, J. Vac. Sci. Technol. B **12**, 1217 (1994).

[59] C. Lu and Y. Guan, J. Vac. Sci. Technol. A **13**, 1797 (1995).

[60] W. Wang, R. H. Hammond, M. M. Fejer, and M. R. Beasley, J. Vac. Sci. Technol. A **17**, 2676 (1999).

[61] B. Utz, S. Rieder-Zecha, and H. Kinder, IEEE Trans. Appl. Supercond. **7**, 1181 (1997).

[62] Y. Du, T. C. Droubay, A. V. Liyu, G. Li, and S. A. Chambers, Appl. Phys. Lett. **104**, 163110 (2014).

[63] X. He and M. Razeghi, J. Appl. Phys. **73**, 3284 (1993).

[64] M. A. Zurbuchen, Y. Jia, S. Knapp, A. H. Carim, D. G. Schlom, and X. Q. Pan, Appl. Phys. Lett. **83**, 3891 (2003).

[65] Y. Iwazaki, T. Suzuki, S. Sekiguchi, and M. Fujimoto, Jpn. J. Appl. Phys., Part 2 **38**, L1443 (1999).

[66] J. H. Haeni, C. D. Theis, D. G. Schlom, W. Tian, X. Q. Pan, H. Chang, I. Takeuchi, and X.-D. Xiang, Appl. Phys. Lett. **78**, 3292 (2001).

[67] W. Tian, X. Q. Pan, J. H. Haeni, and D. G. Schlom, J. Mater. Res. **16**, 2013 (2001).

[68] W. Tian, J. H. Haeni, D. G. Schlom, E. Hutchinson, B. L. Sheu, M. M. Rosario, P. Schiffer, Y. Liu, M. A. Zurbuchen, and X. Q. Pan, Appl. Phys. Lett. **90**, 022507 (2007).

[69] M. Jungbauer, S. Hühn, R. Egoavil, H. Tan, J. Verbeeck, G. Van Tendeloo, and V. Moshnyaga, Appl. Phys. Lett. **105**, 251603 (2014).

[70] R. C. Haislmaier, G. Stone, N. Alem, and R. Engel-Herbert, Appl. Phys. Lett. **109**, 043102 (2016).

[71] K. Hawkins and T. White, Philos. Trans. R. Soc. London **336**, 541 (1991).

[72] T. Williams, F. Lichtenberg, A. Reller, and G. Bednorz, Mater. Res. Bull. **26**, 763 (1991).

[73] M. A. Mccoy, R. W. Grimes, and W. E. Lee, Philos. Mag. A **75**, 833 (1997).

[74] R. Seshadri, M. Hervieu, C. Martin, A. Maignan, B. Domenges, B. Raveau, and A. N. Fitch, Chem. Mater. **9**, 1778 (1997).

[75] J. Sloan, P. D. Battle, M. A. Green, M. J. Rosseinsky, and J. F. Vente, J. Solid State Chem. **138**, 135 (1998).

[76] T. Suzuki, Y. Nishi, and M. Fujimoto, J. Am. Ceram. Soc. **83**, 3185 (2000).

[77] W. Kwestroo and H. A. M. Paping, J. Am. Ceram. Soc. **42**, 292 (1959).

[78] T. Suzuki and M. Fujimoto, J. Appl. Phys. **89**, 5622 (2001).

[79] Y. Tokura and T. Arima, Jpn. J. Appl. Phys., Part 1 **29**, 2388 (1990).

[80] S. Hendricks and E. Teller, J. Chem. Phys. **10**, 147 (1942).

[81] B. Aurivillius, Ark. Kemi **1**, 499 (1950).

[82] B. Aurivillius, Ark. Kemi **2**, 519 (1951).

[83] B. Aurivillius, Ark. Kemi **5**, 39 (1953).

[84] B. Aurivillius and P. H. Fang, Phys. Rev. **126**, 893 (1962).

[85] B. Aurivillius, Ark. Kemi **1**, 463 (1950).

[86] M. A. Zurbuchen, R. S. Freitas, M. J. Wilson, P. Schiffer, M. Roeckerath, J. Schubert, M. D. Biegalski, G. H. Mehta, D. J. Comstock, J. H. Lee, Y. Jia, and D. G. Schlom, Appl. Phys. Lett. **91**, 033113 (2007).

[87] M. A. Zurbuchen, V. O. Sherman, A. K. Tagantsev, J. Schubert, M. E. Hawley, D. D. Fong, S. K. Streiffer, Y. Jia, W. Tian, and D. G. Schlom, J. Appl. Phys. **107**, 024106 (2010).

[88] M. A. Zurbuchen, N. J. Podraza, J. Schubert, Y. Jia, and D. G. Schlom, Appl. Phys. Lett. **100**, 223109 (2012).

[89] M. A. Zurbuchen, D. G. Cahill, J. Schubert, Y. Jia, and D. G. Schlom, Appl. Phys. Lett. **101**, 021904 (2012).

[90] J. B. Nelson and D. P. Riley, Proc. Phys. Soc. **57**, 160 (1945).